Available online at www.sciencedirect.com
SCIENCE DIRECT®
Nuclear Instruments and Methods in Physics Research A 541 (2005) 365–371
NUCLEAR INSTRUMENTS & METHODS IN PHYSICS RESEARCH Section A
www.elsevier.com/locate/nima

The ground calibration of X-ray CCD cameras (XIS) with front-illuminated chips onboard Astro-E2

H. Nakajima[a,*], H. Yamaguchi[a], H. Matsumoto[a], T.G. Tsuru[a], K. Koyama[a], S. Kissel[b], B. LaMarr[b], M. Bautz[b]

[a]*Department of Physics, Graduate School of Science, Kyoto University, Oiwake-cho Kitashirakawa Sakyo-ku, Kyoto 606-8502, Japan*
[b]*Center for Space Research, Massachusetts Institute of Technology, 77 Massachusetts Avenue Cambridge, MA 02139-4307, USA*

Available online 23 February 2005

Abstract

We report on the results of the ground calibration of Astro-E2/XIS with front-illuminated (FI) chips. The sensors have basically the same performance as that of Astro-E/XIS. However, there are some improved points: (1) A ^{55}Fe radio isotope is equipped on the door and (2) the capability for charge injection (CI) has been added. We measured the gain, energy resolution, and quantum efficiency (QE) of the FI sensors as a function of energy by using characteristic X-rays for each sensor. An energy resolution of 130 eV at 5.9 keV in FWHM and a QE of 52% at 8.6 keV are achieved. After XIS is launched, the charge transfer inefficiency (CTI) will increase due to radiation damage by cosmic rays. Then XIS is equipped with the CI capability to calibrate and compensate for the increase in CTI. We estimate the time variability in the amount of the injected charge.

PACS: 95.55.Aq; 95.55.Ka

Keywords: X-ray telescope; Astro-E2; X-ray; CCD; XIS; Calibration

1. Introduction

Astro-E2 is the successor to the Astro-E [1,2], the 5th Japanese X-ray satellite, which failed to achieve orbit in 2000. It will be launched in 2005 and put into a low earth orbit. Onboard detectors are followings: the X-ray micro-calorimeter referred to as X-Ray Spectrometer (XRS), Hard X-ray Detector (HXD), and the X-ray CCD Camera referred to as X-ray Imaging Spectrometer (XIS). XRS has the extremely high-energy resolution of 6 eV at 5.9 keV in FWHM (20 times better than X-ray CCDs) and moderate imaging capability (6×6

*Corresponding author. Tel.: +81 75 753 3851; fax: +81 75 753 3799.
E-mail address: Nakajima@cr.scphys.kyoto-u.ac.jp (H. Nakajima).

0168-9002/$ - see front matter © 2005 Elsevier B.V. All rights reserved.
doi:10.1016/j.nima.2005.01.077

pixels in the field of view of $3'.2 \times 3'.2$). HXD consists of phoswitch scintillation counters (GSO, BGO) and PIN photo-diodes. It has the highest sensitivity among all past and present detectors in the hard X-ray band (10–200 keV) and has a large energy range (8–600 keV) [3]. We will describe XIS in detail in Section 2. XRS and XIS are placed at the focal plane of the X-Ray Telescope (XRT). Thanks to the superior light condensing power of XRT, XIS has a larger effective area than competing *Chandra*/ACIS and *XMM*/EPIC in the high-energy band ($\geqslant$11 keV). Utilizing these detectors, Astro-E2 has an advantage over *Chandra* and *XMM* in its wide energy range and capability for high-resolution spectroscopy. Astro-E2 also has an advantage with respect to background conditions since cosmic ray induced background is considered to be lower in low earth orbit than in the high earth orbit of *Chandra* and *XMM*.

X-ray photon-counting CCDs have loaded into the satellite for the first time in *ASCA*. High-position resolution, wide energy range, high quantum efficiency (QE), and moderate energy and time resolution have made X-ray CCDs the standard detector in X-ray astronomy. XIS is only one of the detectors onboard Astro-E2 which can determine the position of X-ray source precisely.

All sensors of XIS were developed through the collaboration of the Center for Space Research, (CSR) at Massachusetts Institute of Technology (MIT), the Japan Aerospace Exploration Agency (JAXA)/Institute of Space and Astronautical Science (ISAS), Osaka University, Kyoto University, Rikkyo University, Kogakuin University, and Ehime University. The Analog Electronics (AE) and CCD chips were developed at CSR and the Lincoln Laboratory at MIT, respectively. The upper part of the sensors (hereafter referred to as bonnet) and Digital Electronics (DE) were developed by JAXA/ISAS, Osaka University, and Kyoto University.

The CCD calibration was done by MIT, Osaka University and Kyoto University. Gain, energy resolution, QE, and charge injection (CI) capability (described in Section 2) were investigated. After a simple calibration at MIT, Osaka University group investigated the low energy ($\leqslant$Si edge $\simeq$ 1.8 keV) X-ray response of the sensors. At Kyoto University, the focus was the high energy ($\geqslant$Al Kα line $\simeq$ 1.5 keV) response.

In this paper, after a simple description of XIS in Section 2, the goal of the calibration will be explained (Section 3). Section 4 describes the results of that calibration, and is followed by the summary in Section 5.

2. Description of XIS

XIS consists of the sensor, AE, and DE. The sensor is shown in Fig. 1. The readout analog signals from the sensor are transferred to AE and converted into the digital signals. The digitized pixel data are transferred into DE and then each X-ray event is extracted. The X-ray event information is formatted into telemeter data and transferred to the data processor.

XIS has four sets of CCD cameras, three sets of which utilize front-illuminated (FI) chips, while the other is equipped with back-illuminated chip. All sensors including spares utilize the three phase CCD and the FI CCDs (hereafter referred to as FI0–FI3) have basically the same chip structure as the ACIS-I chips onboard *Chandra* [4]. Pixel size and pixel number are 24 μm × 24 μm and 1024 × 1024, respectively. The time resolution is 8 ms for timing mode and 8 s for normal mode. There are four readout nodes and each divided region is called as Segment A–D. CCDs generally suffer from dark current due to the thermal excitation of electrons and the small energy band gap of Si semiconductor crystals (1.12 eV). Therefore, the chip is cooled to $-90\,^{\circ}$C by the thermo electric cooler (TEC; Peltier sensor). X-ray CCDs are also sensitive to optical light. The XIS sensor equips the optical blocking filter (OBF) right above the chip. The OBF has a low-transmission rate for optical light ($\leqslant 5 \times 10^{-5}$) and a high X-ray transmission rate ($\simeq$ 70% for O KX line). The OBF is fragile so vibrations during launch may destroy it; at the time of the launch, the vicinity of the chip and the OBF will be kept in an air-tight vacuum by closing a door equipped with the bonnet. Furthermore, a ^{55}Fe calibration source is equipped on the door. The aim of this source

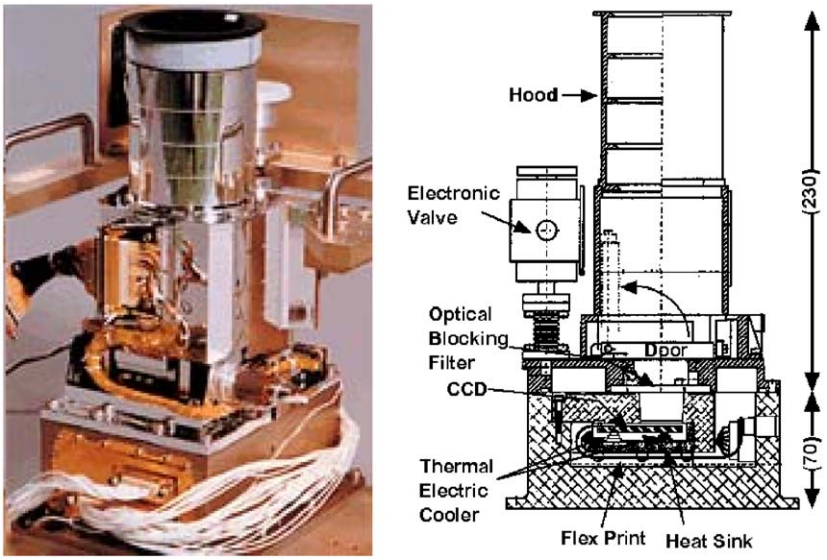

Fig. 1. Left: An outside view of XIS sensor component. Right: Schematic view of XIS sensor component. The single-hatched and cross-hatched regions are bonnet and base, respectively.

is to measure changes in the performance of the CCD from the time of launch to the time of the door opening. The source shines X-rays on the whole chip almost uniformly until the door is opened.

As for the chip, a CI capability has been added. In orbit, some elements of the performance of the CCD are affected by radiation damage from cosmic rays. ACIS and EPIC suffer from degradation due to the low-energy ($\sim$ 10–100 keV) solar protons [5,6]. In order to maintain the performance of CCDs in orbit, the CTI must be frequently measured and corrected. Furthermore, *ASCA*/SIS left an assignment: the CTI differs significantly along the columns, therefore, some capability is needed such that the CTI can be measured for each column. A serial register has been equipped above the imaging area for Astro-E2/XIS (Fig. 2). From the input diode at the end of the register, an amount of charge is positioned throughout the register. The charges are then injected into the imaging area and read. The amount of injected charge can be made constant by controlling the voltage between the electrode in the register and input gate, allowing the CTI to be measured column by column.

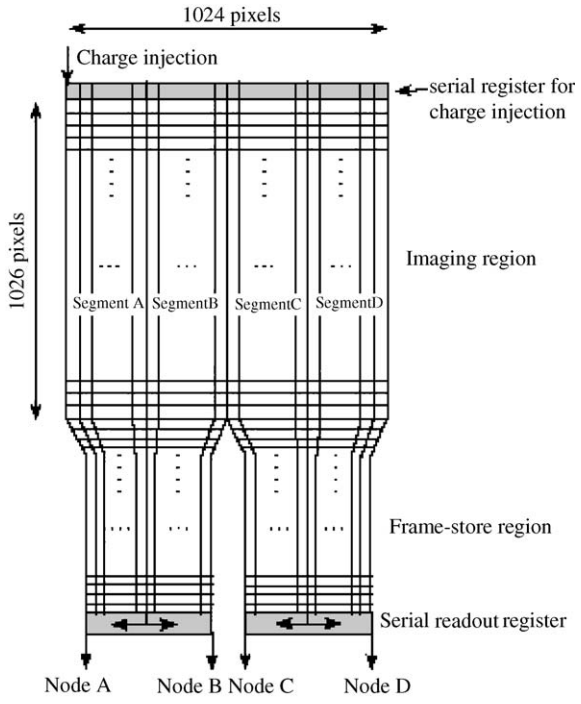

Fig. 2. A schematic view of the CCD chip. A serial register is equipped at the top of the imaging area for CI capability. The chip has four read-out nodes. Signals are read-out simultaneously from these nodes.

3. Calibration goal

Fig. 3 shows a spectrum of ^{55}Fe obtained with the XIS Flight Model (FM) FI1 sensor. In it, we can see not only the main peaks of Mn Kα and Kβ, but also the escape peaks, fluorescent peak, tail, and constant component. The ratio of the intensity of these components to one another is sensitive to the X-ray energy, gate structure, and the depth of depletion layer. In order to interpret X-ray spectra obtained in orbit, we aim to construct a precise response distribution function for monochromatic X-rays.

The goals of our calibration are as follows: (1) Gain as a function of incident X-ray energy should be measured with an error of $<0.1\%$, (2) the energy resolution should be determined with an accuracy of 1%, (3) the QE should be determined with an accuracy of 10%, and finally (4) the spectral shape of monochromatic X-rays, including the Si fluorescent peak, escape peaks, tail, and constant component should be measured with errors of $<3\%$.

4. Calibration results

4.1. Calibration system

The calibration was conducted with the fluorescent X-ray generation system at Kyoto University [7]. The X-ray generation system involves continuous X-rays from an X-ray generator which shine an selected target within a chamber. The targets (Al, Cl, Ti, Fe, Zn, Se, and Polyethylene) are on a rotating stage. Secondary fluorescent X-rays are incident on XIS in the other chamber. In the case that XIS is moved out of the beam line, the intensity can be measured and a spectrum of the beam can be taken using a backward windowless solid-state detector (SSD).

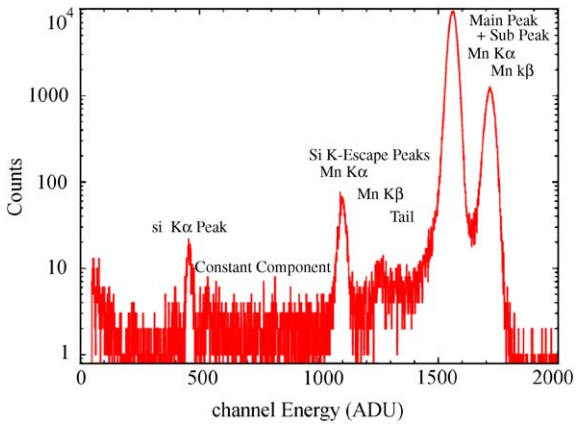

Fig. 3. A spectrum of the XIS FI sensor for the ^{55}Fe source. There are several components in this spectrum such as the main peak, subpeak, constant component, escape peak, and Si Kα peak, all of which are labeled. The final purpose of calibration is to determine the flux of each component to within an error of less than 3%.

During the calibration, the sensor was in an environment such that the pressure was $\sim 2\times 10^{-6}$ Torr and the CCD temperature was $\sim -90\,^{\circ}$C. In the following, we describe the results of our calibration.

4.2. Readout noise

First, we investigated the readout noise of each sensor segment. All sensors showed noise levels of $\sim$ 2–3 ADU (RMS). From these values, we determined the threshold for event extraction. XIS utilizes the same event extraction method as *ASCA*/SIS. Depending on the spread pattern of the charge, the "grade" of each event is determined. The details of the *ASCA* grade are explained in NASA's Research Announcement NRA 93-OSS-08. If the event belongs to grades 0, 2, 3, 4, or 6, the event is regarded as an X-ray event. Then the pixel levels are summed over the pixel whose pixel level is larger than the split threshold. Therefore, in order to measure the pulse height correctly, it is essential to determine the value of the split threshold considering the readout noise. The noise level is 2–3 ADU, so $\sim$ 12 ADU, i.e. $\sim 4\sigma$ of the readout noise [8] is preferable as the split threshold. We then set the threshold to be 20 ADU considering the margin.

4.3. Gain

Adopting the split threshold determined in the above section, we extracted the X-ray events from each data set and made a spectrum. For the line spectrum of each fluorescent X-ray, we fitted each peak with two Gaussians considering the response distribution function. Fig. 4 shows the gain of XIS FI1 segment A. The grade of the extracted events

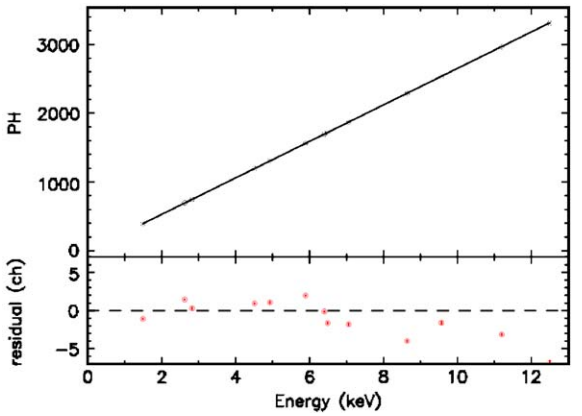

Fig. 4. The XIS energy scale linearity. The data was taken with the XIS FI1 segment A. We obtained a gain of 265.1 ch/keV.

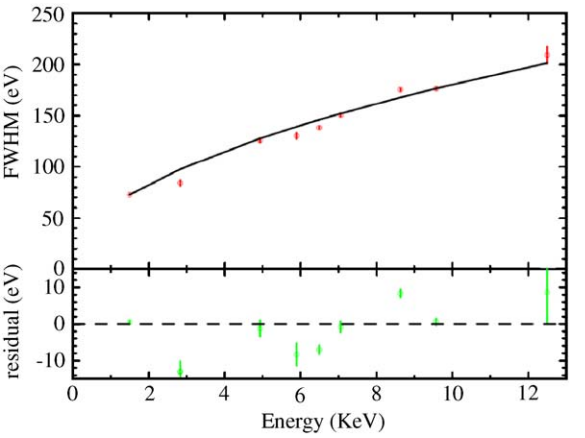

Fig. 5. The spectral resolution as a function of energy for the XIS FI1 segment A. We obtained a resolution of 131 eV in FWHM at 5.89 keV.

are 0, 2, 3, 4, or 6. The energy–pulse-height relation is quite linear in the energy band of 1–12 keV. The error of the gain is less than 0.1% for all segments of all sensors. The difference in gain among the segments is less than 10%.

4.4. Energy resolution

Fig. 5 shows the spectral resolution of XIS FI1 segment A. The grades of the extracted events are the same as in the previous section. We fitted the data with the following function:

$$\Delta E(\mathrm{eV}) = W\sqrt{8\ln 2}\sqrt{N^2 + \frac{EF}{W}} \quad (1)$$

where E, F, W, and N are the X-ray energy in eV, the Fanofactor, the mean electron–hole pair creation energy of Si (3.65 eV), and the RMS system noise that consists of readout noise and dark current, respectively. The free parameters are N and F/W. The best-fit value of N and F/W are 2.6 ± 1.2 electrons and $4.34 \pm 0.06 \times 10^{-2}$, which correspond to the Fanofactor of $\sim 1.58 \pm 0.02$. Considering the gain obtained in the previous section, the values for the noise and Fanofactor are consistent with the results of Section 4.2 considering the dark current of ~ 1—3 electron frame pixel and with the literature [9]. We achieve an energy resolution of ~130 eV at 5.9 keV for all sensors. The error in the resolution is less than 1% for all segments of all sensors.

4.5. Quantum efficiency

Fig. 6 shows the QE of XIS FI1 segment A. The solid curves represent the simulated function with a simple layer model. The central curve assumes nominal values for the thickness of the electrode layer, insulation layer, and depletion layer, that is, 0.33, 0.27, and 74 μm, respectively. The uppermost and lowermost curves represent the cases when the thickness of each layer deviates from the nominal value by $\sim \pm 10\%$; if we assume that the electrode and insulation layer is thicker than in the nominal case, the QE in the soft energy band will be lower. Besides, assuming that the depletion layer is thicker than in the nominal case, the QE in the hard energy band will be higher. We can see that the QE of XIS at ~ 4.5 keV (Ti Kα line) is $96\pm0.7\%$, regardless of the thickness of each layer.

First we made spectra of XIS and windowless SSD, which is located behind XIS. Since the QE of the SSD is $\sim 100\%$, we measured the normalized QE of XIS as a function of the intrinsic energy, and $\sim 52\%$ at 8.6 keV is achieved. The error in the normalized QE is less than 3% for all segments of all sensors.

4.6. Charge injection capability

In order to test the CI capability, the stability of the injected charges was investigated; time variability of the charge injected in the specified pixel and the amount of charge between the columns were investigated because the stable injection of the charge is essential to measure the CTI of each column.

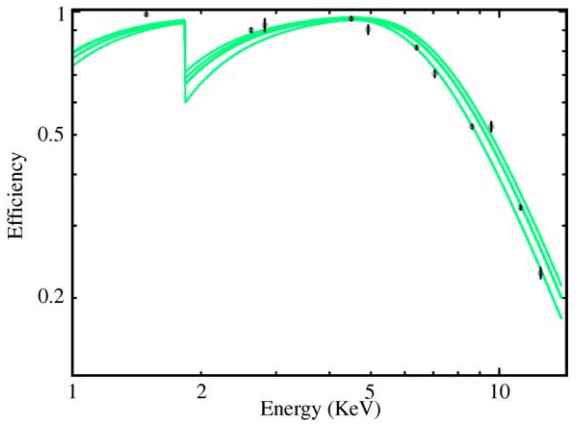

Fig. 6. The QE as a function of energy for XIS FI1 segment A. The solid curves show simulated QE, where the input parameters are the thickness of the electrode layer, insulation layer, and depletion layer. We determined the nominal value to be 0.33 (0.25–0.45) μm, 0.27 (0.20–0.35) μm, and 74 (60–80) μm, respectively. Having confirmed that the QE at 4.5 keV is almost constant ($96 \pm 0.7\%$), we normalized the QE to 96% at 4.5 keV.

350 frames of data (2800 s) were taken with injected charges. Fig. 7 shows a frame image of injected charges. We controlled the injection pattern so that the charges could be detected as events and injected into one pixel per column. Then, we make a histogram of the pulse-height distribution of the charges injected in a specified pixel. We fitted this histogram with a Gaussian model. The peak centroid and peak width correspond to an X-ray with an energy of 4.5 keV and FWHM of 85 eV ($\sim 70\%$ of X-rays). This confirms the stability of the injected charge in the specified pixel.

Then, we investigated whether the pulse height of injected charge of a column reflects the CTI of the column. Fig. 8 shows the correlation between the pulse height of injected charges and those of the ^{55}Fe events for each column. The ^{55}Fe events were extracted from the upper-half of the imaging area in order that the pulse height of the events may reflect the CTI of each column, allowing the investigation of a large number of events. We cannot see a positive correlation between the two data sets; the line fit results in a slope of ~ 0.04. While the pulse-height dispersion of the ^{55}Fe events is exceedingly small, the dispersion of injected charge is rather large. We cannot say that the pulse heights of injected charges simply represent the CTI of each column. Our next goal is to determine how to best measure the CTI using the CI capability in the onboard environment.

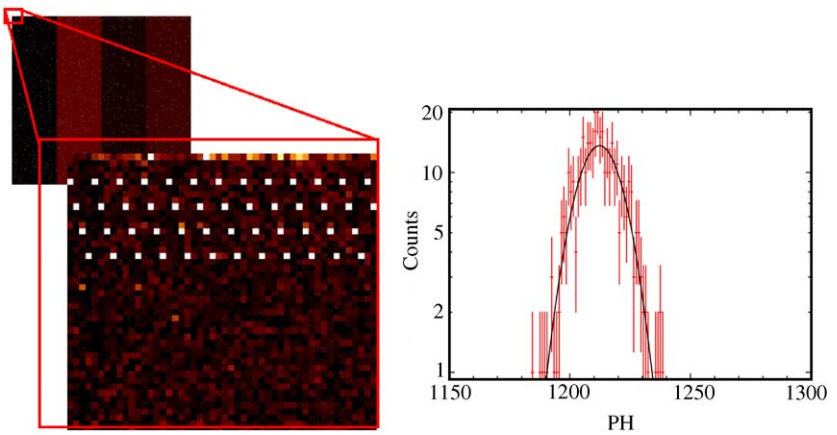

Fig. 7. Left: The false color frame image of XIS FI1 during charge injection. Right: A histogram of the pulse height distribution of the charge injected to a specified pixel. The histogram is made from 350 frames of data.

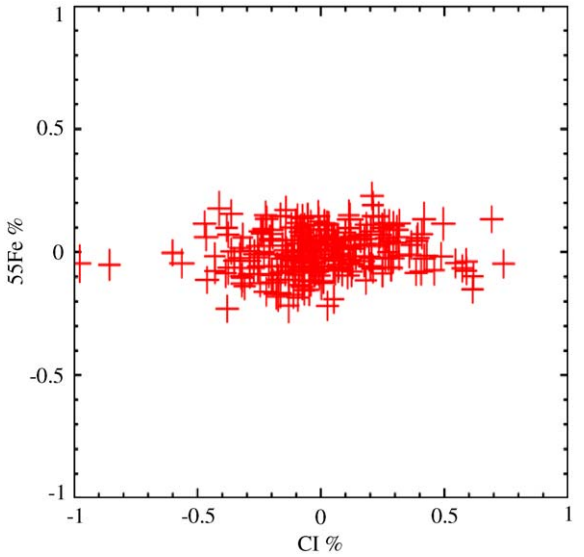

Fig. 8. The correlation between the pulse height of the injected charges of each column and those of the ^{55}Fe events. The ^{55}Fe events were extracted from the upper-half of the imaging area. The units on both axes are the percentages of the deviation from the mean value of the pulse height.

5. Summary

We have reviewed the ground calibration conducted at Kyoto University of the FM FI sensors of XIS onboard Astro-E2. The basic performances of the X-ray CCD, such as the gain, energy resolution and QE were derived. An energy resolution of 130 eV at 5.9 keV in FWHM and a QE of 52% at 8.6 keV were achieved. Calibration was successful in these three areas, since the error for each parameter is $<0.1\%$, $<1\%$, and $<3\%$, respectively. The preliminary results regarding the feasibility of the CI capability are also presented. The stability of the amount of injected charge in a specified pixel is confirmed. However, as for the variability between pixels, the consistency between the pulse height of CI events and ^{55}Fe events cannot be confirmed. We plan to conduct extra calibration using the engineering unit sensor having larger CTI than the FM sensors.

Acknowledgements

The authors express their special thanks to all the member of the XIS team. H.N. was financially supported by the Japan Society for the Promotion of Science.

References

[1] K. Mitsuda, Astronomische Nachrichten 320 (1999) 273.
[2] H. Inoue, Adv. Space Res. 32 (2003) 2089.
[3] C. Tanihata, J. Kataoka, T. Murakami, N. Ota, H. Ozawa, T. Takahashi, T. Tamura, Y. Uchiyama, S. Watanabe, K. Yamaoka, D. Yonetoku, Y. Ezoe, Y. Fukazawa, N. Isobe, N. Iyomoto, Proc. SPIE 3765 (1999) 645.
[4] M. Bautz, S. Kissel, G. Prigozhin, Y. Gregory, S. Jones, T. Isobe, H. Manning, M. Pivovaroff, G. Ricker, J. Woo, Proc. SPIE 2808 (1996) 170.
[5] P.P. Plucinsky, S.N. Virani, Proc. SPIE 4012 (2000) 681.
[6] A.M. Read, T.J. Ponman, Astron. Astrophys. 409 (2003) 395.
[7] K. Hamaguchi, Y. Maeda, H. Matsumoto, M. Nishiuchi, H. Tomida, K. Koyama, H. Awaki, T.G. Tsuru, Nucl. Instr. and Meth. A 450 (2000) 360.
[8] K. Imanishi, H. Awaki, T.G. Tsuru, K. Hamaguchi, H. Murakami, M. Nishiuchi, K. Koyama, Proc. SPIE 4012 (2000) 137.
[9] G.F. Knoll, Radiation Detection and Measurement, Wiley, New York, 1989, p. 340.